

# 1 Retrieving Stratospheric Ozone Profiles from OMPS Limb

## 2 Profiler Measurements

3 Fang Zhu<sup>1</sup>, Xiaoping Liu<sup>1</sup>, Suwen Li<sup>1</sup>, Fuqi Si<sup>2</sup>

4 <sup>1</sup>Anhui Province Key Laboratory of Pollutant Sensitive Materials and Environmental Remediation, Anhui Province Key  
5 Laboratory of Intelligent Computing and Applications, School of Physics and Electrical Information, Huaibei Normal  
6 University, Huaibei, 235000, Anhui, China

7 <sup>2</sup>Centre of Environmental Optics, Anhui Institute of Optics and Fine Mechanics, Hefei Institutes of Physical Science,  
8 Chinese Academy of Sciences, Hefei, Anhui 230031, China

9  
10 *Correspondence to:* Fang Zhu (zhufang160@163.com)

11 **Abstract.** This study presents an independent retrieval algorithm combining wavelength pairing and the multiplicative  
12 algebraic reconstruction technique (MART) to process Ozone Mapping and Profiler Suite (OMPS) limb observations for  
13 vertical ozone profiles. Developed as a complementary dataset for validating operational products, the algorithm is  
14 tailored to OMPS limb profiler's specific characteristics. The retrieval algorithm employs scattered solar radiance  
15 measurements from the OMPS/LP, focusing on the visible spectral range, normalizes this radiance to that at an upper  
16 tangent height, and retrieves ozone concentrations between 12–40 km. Additionally, it enables the identification of  
17 cloud-contaminated measurements at specific altitudes within the instrument field of view. A comprehensive error  
18 analysis reveals that prior uncertainty contributes ~5% error in the tropical lower stratosphere (based on a +5%  
19 perturbation experiment), while a 30% uncertainty in the aerosol extinction coefficient causes ~5% error at 15–25 km.  
20 Absorption cross-section uncertainties introduce localized biases of –3% to –5%, and random measurement noise  
21 exhibits strong altitude dependence, with values below 10% in the mid-stratosphere and exceeding 20% at high altitudes  
22 and in the tropical upper troposphere. OMPS data spanning the entire year of 2021 are processed, and the results are  
23 evaluated through comparisons with multiple independent datasets, including NASA official products, passive satellite  
24 observations, and in-situ measurements from balloon-borne ozonesondes. At 17–36 km, deviations from OMPS/LP v2.6  
25 data are  $\leq 5\%$ ; at 18–35 km, consistency with Microwave Limb Sounder (MLS) v5.0 data ranges from 5–10%; at 20–35  
26 km, most deviations from OSIRIS v7.3 data are  $\leq 5\%$  (except near 23 km). Comparisons with ozonesonde  
27 measurements reveal that differences in the 13–30 km range over northern mid-to-high latitudes are mostly  $< 10\%$  (with  
28 10–15% differences at 22–25 km in polar regions). Over southern mid-latitudes, the consistency within the same altitude  
29 range is 2–10%. Notably, deviations between the retrieved profiles and comparison products increase significantly in the  
30 tropics at low altitudes.

### 31 1 Introduction

32 Stratospheric ozone forms a natural barrier protecting life on Earth by absorbing solar ultraviolet (UV) radiation.  
33 Additionally, as a key greenhouse gas, it participates in the absorption and emission of infrared radiation in the  
34 stratosphere, playing a crucial role in regulating Earth's energy balance and stabilizing the climate system (Li, F., et al.,  
35 2023). Dynamic changes in stratospheric ozone concentrations not only directly reflect the emission fluxes and chemical  
36 reaction processes of various atmospheric substances, but also serve as an important indicator for assessing the impact of  
37 human activities on the atmospheric environment (Young et al., 2021; Chipperfield and Bekki, 2024). Since the

38 identification of the Antarctic ozone hole in the 1980s, research on the evolution patterns and driving mechanisms of  
39 stratospheric ozone concentration has remained a core topic in atmospheric science, attracting global research efforts to  
40 continuously explore its variation mechanisms and ecological effects.

41 High-precision retrieval of stratospheric ozone vertical profiles is a core requirement for advancing stratospheric  
42 ozone research and establishing long-term essential climate variable datasets (Jia et al., 2015). To this end, multi-platform  
43 monitoring technologies—including ground-based, balloon-borne, airborne, and satellite-based instruments—have been  
44 widely applied over recent decades. Among these, satellite observations are categorized by detection modes into nadir,  
45 occultation, and limb observations. Nadir-viewing instruments, which observe downward, offer excellent horizontal  
46 coverage, with typical examples including the Ozone Monitoring Suite–Nadir (OMS-N) aboard Fengyun-3F  
47 (NSMC,2025), the Ozone Monitoring Instrument (OMI) aboard Aura(Veefkind et al., 2006), and the Environmental  
48 Monitoring Instrument (EMI) onboard the hyperspectral observation satellite GeoFen-5 (Qian et al., 2024). Occultation  
49 instruments, which directly view the solar disk, are represented by the Stratospheric Aerosol and Gas Experiment (SAGE  
50 III) (Cisewski et al., 2014), Atmospheric Chemistry Experiment (ACE) (Bernath et al., 2005), and Global Ozone  
51 Monitoring by Occultation of Stars (GOMOS) (Bertaux et al., 2010), featuring high vertical resolution and good  
52 signal-to-noise ratio. Limb scattering/emission observations combine the advantages of the aforementioned two modes,  
53 boasting high sensitivity, favorable vertical resolution, and high spatial sampling rates, such as the Microwave Limb  
54 Sounder (MLS) (Waters et al., 2006), SCanning Imaging Absorption spectroMeter for Atmospheric CartographY  
55 (SCIAMACHY) (Burrows et al., 1995), and Optical Spectrograph and InfraRed Imager System (OSIRIS) (Llewellyn et  
56 al., 2004). The Ozone Mapping and Profiler Suite (OMPS), a passive imaging spectrometer employed in this study, is  
57 onboard the Suomi-National Polar-orbiting Partnership (SNPP) satellite (Flynn et al. 2014). Its limb profiler (OMPS/LP)  
58 enables accurate retrieval of stratospheric ozone vertical profiles via limb observation mode. Since 2012, the NASA team  
59 has successively developed and released four versions of the ozone LP retrieval algorithm for OMPS limb observation  
60 data (the first version was released (Rault et al,2013), the second version in 2014 (Xu et al.,2014), version 2.5 in 2017  
61 (DeLand et al., 2017), and version 2.6 in 2023(Kramarova, 2023)). The University of Bremen has also applied its  
62 self-developed retrieval algorithm to OMPS/LP measurements (Arosio et al., 2018). In addition, another approach to  
63 processing OMPS/LP data employs a 2-D geometry retrieval method, as demonstrated in the work conducted at the  
64 University of Saskatchewan (Zawada et al., 2018).

65 This study focuses on ozone profile retrieval from OMPS/LP observation data, employing a retrieval algorithm  
66 based on wavelength pairing and the multiplicative algebraic reconstruction technique (MART). The algorithm is derived  
67 from the OSIRIS ozone profile retrieval scheme developed by the University of Saskatchewan. While the core retrieval  
68 methodology of wavelength pairing and MART is well-established in limb sounding, the novelty of this work lies in its  
69 tailored adaptation to the OMPS/LP instrument. Given the significant differences between OMPS/LP and OSIRIS in  
70 measurement technologies—including spectral resolution, spectral channels, wavelength range, atmospheric sampling,  
71 and radiance acquisition—this study has performed targeted optimizations and innovations on the algorithm. These  
72 include significant adaptations in radiative transfer model construction, selection of retrieval spectra, and application of  
73 atmospheric parameter databases. Furthermore, this study provides an independently developed retrieval pathway for  
74 OMPS/LP, offering a complementary source for cross-validation with official products.

75 The study aims to demonstrate the effectiveness of the wavelength pairing and MART algorithm for retrieving  
76 OMPS/LP ozone profiles, thereby laying a theoretical and technical foundation for integrating OMPS/LP and OSIRIS  
77 data to construct long-term continuous datasets. The structure of this paper is as follows: Section 2 details the  
78 characteristics of the OMPS instrument, discussing its observational geometric principles and key issues in L1 data  
79 calibration. Section 3 systematically elaborates on the retrieval algorithm, including its core framework, application  
80 strategy of cloud filters, and parameter setting methods for the radiative transfer model. Section 4 conducts  
81 multi-dimensional validation and statistical analysis of the retrievals in this study, against NASA ozone profile products,

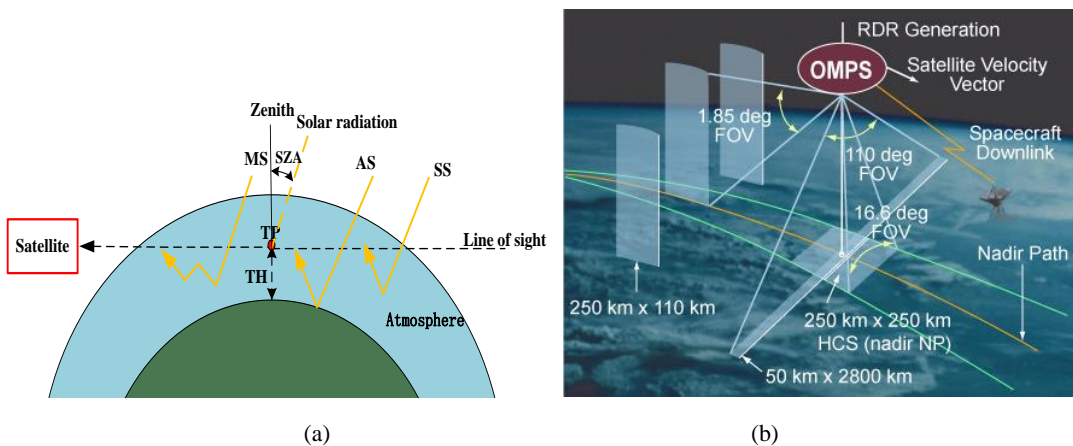
82 MLS, OSIRIS, and ozonesonde datasets. Finally, the main results, key findings are summarized, and potential directions  
 83 for future algorithm improvement are outlined in the conclusions.

## 84 2 OMPS/LP Ozone Retrieval

### 85 2.1 OMPS/LP instrument

86 The OMPS instrument was successfully launched aboard the SNPP satellite on October 28, 2011 (Zhu et al., 2025).  
 87 The satellite operates in a sun-synchronous polar orbit at an average altitude of 833 km with a 13:30 local time ascending  
 88 node, commencing routine scientific observations in early 2012 (Kramarova et al., 2022). The OMPS suite integrates  
 89 three distinct sensors: the Nadir Mapper (NM), Nadir Profiler (NP), and Limb Profiler (LP) (Flynn et al., 2014). Among  
 90 them, OMPS/LP is centrally aimed at retrieving the vertical distribution of ozone in the Earth's middle atmosphere with  
 91 high precision, employing a limb observation mode to sound the atmosphere by imaging the edge of the Earth's  
 92 atmosphere. During a limb observation, the sensor's line-of-sight passes tangentially through the atmosphere, and the  
 93 point along this path with the lowest altitude is termed the tangent point (TP). The vertical distance from this point to the  
 94 Earth's geoid is referred to as the tangent height (TH). The fundamental geometry of this observation mode is depicted in  
 95 Fig. 1a.

96 The spectral coverage of OMPS/LP ranges from 290 nm to 1000 nm, with spectral resolution varying with  
 97 wavelength from 1.5 nm at short wavelengths to 40 nm at the longer-wavelengths (Kramarova et al., 2014). Equipped  
 98 with a charge-coupled device (CCD), the instrument can simultaneously observe scattered solar radiation across the full  
 99 spectral range at altitudes from 0 to 100 km. Each detector pixel possesses an instantaneous vertical field of view of  
 100 approximately 1.5 km. This configuration enables a high-precision vertical sampling of 1 km at the tangent point. (Jaross  
 101 et al., 2014). To expand cross-track coverage, OMPS/LP is configured with three observation slits horizontally spaced by  
 102  $4.25^\circ$  (approximately 250 km), whose observational geometry and field-of-view characteristics are illustrated in Fig. 1b.  
 103 Each slit has a  $1.85^\circ$  vertical field of view (FOV), corresponding to a 110 km vertical observation range at the TP. This  
 104 study focuses on measurement data from the central slit, which is aligned with the satellite's ground track. The SNPP  
 105 satellite completes 14 orbits daily, with OMPS/LP performing approximately 160–180 measurements per orbit (at a  
 106 latitudinal sampling interval of  $\sim 1^\circ$ ). LP can achieve global coverage every 3–4 days (Kramarova et al., 2024).



107  
 108  
 109 **Figure 1.** (a) Schematic of the satellite limb observation geometry, indicating the key parameters of tangent point (TP) and tangent  
 110 height (TH) (SS: single scattering, AS: albedo scattering, MS: multiple scattering, SZA: solar zenith angle) (adapted from Arosio et al.,  
 111 2018); (b) Schematic diagram of OMPS observation geometry and field-of-view characteristics (Kramarova et al., 2018).

## 112 2.2 Key corrections in OMPS/LP L1G v2.6 data

113 Radiometric errors and sensor pointing errors are the two main error sources affecting limb-scattering ozone  
114 retrieval accuracy (Kramarova et al., 2024). The OMPS/LP L1G v2.6 dataset incorporates essential corrections to address  
115 these issues.

116 Pointing (altitude registration) corrections are applied to mitigate tangent height offsets caused by instrument  
117 alignment and thermal effects. Multi-point corrections include static, intra-orbit, and time-dependent adjustments  
118 following Moy et al. (2017).

119 Stray light correction is performed using an updated point spread function (PSF) based on pre-launch  
120 measurements (Jaross et al., 2014). In version 2.6, the PSF tail intensity in UV and VIS/NIR bands is increased by ~12%  
121 to improve high-altitude stray light estimation (Kramarova et al., 2024). An additional factor of 1.5 is applied in VIS/NIR  
122 wavelengths to correct for in-band scattering. While thermally induced wavelength shifts have negligible impact on  
123 height-normalized radiances in ozone retrieval, we note that residual wavelength-dependent errors could affect  
124 cross-section matching in regions of strong ozone absorption.

125 These calibration steps are critical for ensuring the radiometric and geometric accuracy of the radiances used in  
126 our retrieval. Further details can be found in the cited references.

## 127 3 Retrieval method

### 128 3.1 Retrieval vector

129 The retrieval method for vertical ozone concentration distributions based on OMPS/LP measurements in this study  
130 draws on the technical framework developed by Zhu et al.(2021), who derived ozone number density profiles using  
131 SCIAMACHY limb scattering measurements in the Chappuis–Wulf band. It shares similar methodological principles  
132 with the approaches proposed by Roth et al. (2007) and Degenstein et al. (2009), all of which employ retrieval vectors  
133 positively correlated with ozone concentrations for calculations.

134 The first step in the retrieval process involves normalizing the limb radiance at selected wavelengths. This  
135 operation entails normalizing the limb radiance at each wavelength to a reference TH, which effectively eliminates  
136 interference from the solar Fraunhofer structure, weakens the impact of surface reflection, and simultaneously achieves  
137 instrument self-calibration (Jia et al., 2015).

$$138 I_{\text{nor}}(\lambda, H) = I(\lambda, H)/I(\lambda, H_{\text{ref}}) \quad (1)$$

139 where,  $H$  denotes the TH, and  $\lambda$  represents the wavelength.  $I(\lambda, H_{\text{ref}})$  and  $I_{\text{nor}}(\lambda, H)$  refer to the radiance at the  
140 reference TH and the normalized radiance, respectively. The reference TH is an upper altitude where ozone sensitivity is  
141 low; in this study, it is selected as 40.5 km (i.e., the reference TH above the maximum retrieval altitude). Although  
142 radiance normalization cannot completely eliminate the influence of surface reflection or correct spectral errors such as  
143 wavelength shifts (which affect the calculation of ozone absorption cross-sections), it significantly reduces the  
144 requirements for both absolute radiometric calibration accuracy and modeling accuracy (Flittner et al., 2000). To mitigate  
145 the effect of aerosol scattering, the Chappuis triplet vector (CTV) method proposed by Degenstein et al. (2009) and  
146 Flittner et al. (2000) is employed for wavelength pairing. In the Chappuis-Wulf band, the CTV is defined as the  
147 difference between the logarithmic average of normalized radiances at two weakly ozone-absorbing wavelengths and the  
148 logarithm of the normalized radiance at a wavelength near the ozone absorption peak, thereby isolating the ozone

149 absorption signal from common background scattering effects (e.g., aerosol scattering). It is expressed as:

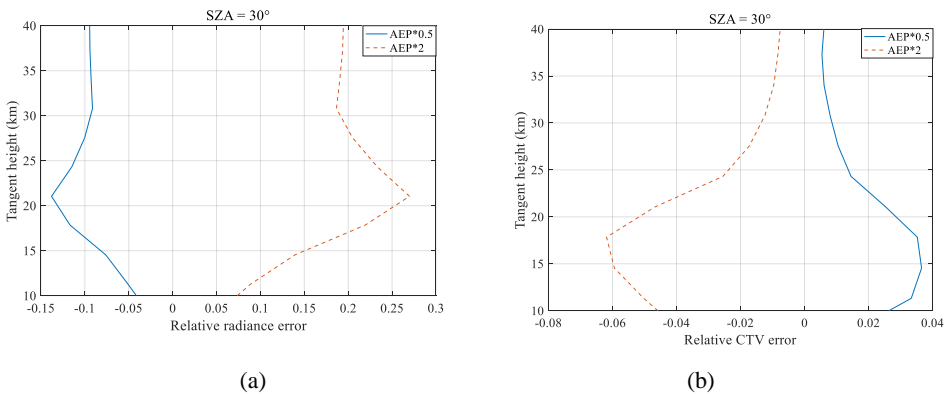
$$150 \quad y_j = \ln \left( \frac{\sqrt{I_{\text{nor}}(\lambda_{\text{ref}1,j}) \cdot I_{\text{nor}}(\lambda_{\text{ref}2,j})}}{I_{\text{nor}}(\lambda_p,j)} \right) \quad (2)$$

151 where,  $j$  denotes the index of the TH measured by the instrument, and  $y_j$  represents the retrieval vector after  
 152 wavelength pairing at the  $j^{\text{th}}$  of TH.  $\lambda_{\text{ref}1}$ ,  $\lambda_{\text{ref}2}$ , and  $\lambda_p$  correspond to the weakly ozone-absorbing reference  
 153 wavelengths and the strongly absorbing peak wavelength, respectively. In this study, the peak wavelength  $\lambda_p=606.3$  nm  
 154 corresponds to the visible channel configuration employed in the NASA OMPS/LP v2.6 operational algorithm  
 155 (Kramarova, et al., 2024), thereby ensuring consistency with established OMPS retrieval products. The weakly absorbing  
 156 reference wavelengths  $\lambda_{\text{ref}1}=512$  nm and  $\lambda_{\text{ref}2}=675.5$  nm were optimized according to the selection criteria proposed by  
 157 Zhu et al. (2021) for limb scattering ozone retrievals within the Chappuis-Wulf band, which take into account the specific  
 158 spectral response and noise characteristics of OMPS/LP. Unlike the NASA algorithm, which uses spectral averages over  
 159 multiple wavelengths for its visible triplet (510 nm, 606 nm, 675 nm; Kramarova and DeLand, 2023), the proposed  
 160 method adopts individual discrete wavelength channels.

161 The CTV is designed to be positively correlated with ozone concentration (Degenstein et al., 2009). As expected, the  
 162 CTV values and the retrieved ozone profiles show consistent vertical and latitudinal variations, with peak altitudes  
 163 decreasing from the tropics to high latitudes. In this study, CTV values near zero above 35 km exhibit insufficient  
 164 sensitivity to ozone, and values above 40 km become negative; therefore, the retrieval is restricted to altitudes below  
 165 40 km.

166 Aerosols, as suspended particles capable of absorbing and scattering light, have sources including both natural and  
 167 anthropogenic factors. Stratospheric aerosols mainly originate from  $\text{SO}_2$ , HCl released by volcanic eruptions, naturally  
 168 generated OCS, and pollutants such as  $\text{SO}_2$  from industrial emissions (Li, Z., et al., 2023). The presence of aerosols  
 169 enhances the intensity of atmospheric scattered light, with the effect being stronger at longer (red) wavelengths than at  
 170 shorter (blue) wavelengths due to wavelength-dependent scattering. Based on the SCIATRAN model (radiative  
 171 TRANSfer model for SCIAMACHY), this study conducted simulation experiments on aerosol extinction coefficients to  
 172 explore their impacts on radiance and CTV.

173 Fig. 2 shows the effects of aerosol extinction profiles perturbed with different scaling factors on radiance and CTV.  
 174 We perturbed the aerosol extinction profiles with factors from 0.1 to 10 and we found that the radiance profile is  
 175 positively correlated with the aerosol extinction coefficient, while CTV decreases as the extinction coefficient increases,  
 176 with the impact mainly concentrated below 30 km. For instance, when the aerosol extinction profile doubles, the radiance  
 177 value at 21 km increases by 27%, while CTV decreases by only 5%. It indicates that wavelength pairing can weaken the  
 178 aerosol scattering effect but cannot completely eliminate it. In addition, the study found that both radiance errors and  
 179 CTV errors increase with an increase in SZA.



180  
 181 **Figure 2.** Variations in radiance and CTV due to perturbed aerosol extinction coefficients.. (a) Relative radiance error; (b) Relative  
 182 CTV error.  
 183

## 184 3.2 Multiplicative algebraic relaxation technology

185 Given the nonlinear nature of the retrieval problem, this study employs an iterative method for solution and selects  
186 the multiplicative algebraic reconstruction technique (MART) to perform ozone profile retrieval. As an improved  
187 algorithm of nonlinear relaxation techniques, MART has a main advantage in that it can utilize multiple sets of  
188 measurement vectors to realize the retrieval of atmospheric state parameters at any altitude (Roth et al., 2007). During the  
189 iteration process, the update of atmospheric states at each altitude depends on a multiplicative factor, which is obtained  
190 by weighted averaging the ratios of all valid observation vectors to simulation vectors. The general formula of the MART  
191 algorithm is as follows:

$$192 \quad x_i^{(n+1)} = x_i^{(n)} \sum_j \left( \frac{y_j^{\text{obs}}}{y_j^{\text{mod}}} W_{ji} \right) = x_i^{(n)} \alpha_i \quad (3)$$

193 where,  $x_i^{(n)}$  denotes the ozone number density at atmospheric height  $i$  during the  $n^{\text{th}}$  iteration;  $y_j^{\text{obs}}$  and  $y_j^{\text{mod}}$   
194 represent the observation vector and simulation vector processed via Equations (1) and (2), respectively, where  $\mathbf{y}^{\text{mod}}$  is  
195 generated by the radiative transfer model based on the ozone profile  $\mathbf{x}^{(n)}$  obtained from the  $n^{\text{th}}$  iteration;  $W_{ji}$  is the  
196 line-of-sight weight factor, indicating the importance of the  $j^{\text{th}}$  TH or line of sight to the ozone retrieved at altitude  $i$ . At  
197 each altitude,  $\sum_j W_{ji} = 1$ . The value of  $W_{ji}$  in this study follows the setting in Zhu et al., (2021).  $\alpha_i$  is the  
198 multiplicative update factors at atmospheric height  $i$ .

199 The sensitivity of retrieval to the true state and the contribution of prior information can be formally described  
200 through the averaging kernel and measurement response (Rodgers, 2000; von Clarmann et al., 2020). However, unlike  
201 Optimal Estimation (OE) approaches, the MART algorithm used in this study does not produce formal averaging kernels.

## 202 3.3 Cloud filter

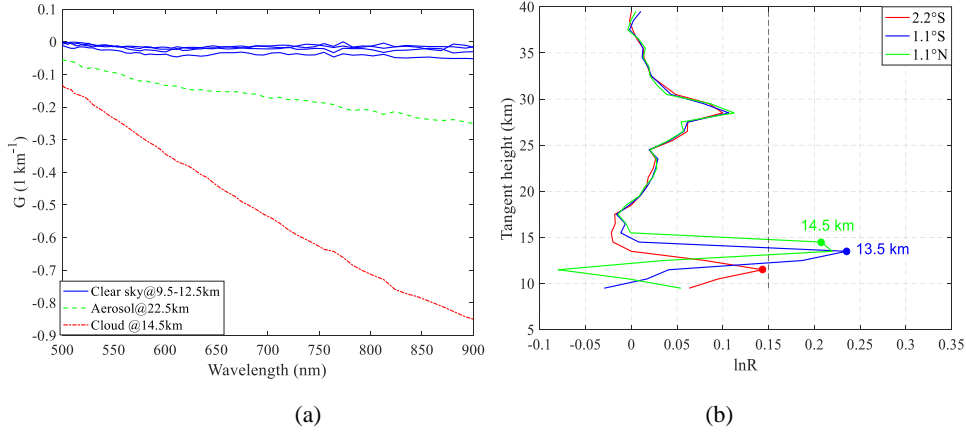
203 A critical step in the OMPS/LP ozone profile retrieval is to define the lower boundary by determining the cloud top  
204 height. This is accomplished using a cloud detection method, modified from Chen et al. (2016), which leverages the  
205 spectral contrast in radiance between red and near-infrared bands. The method quantifies this contrast by computing the  
206 change in the vertical radiance gradient between two selected wavelengths. The underlying premise of the gradient-based  
207 cloud detection algorithm is that clouds generate a significantly larger radiance gradient compared to aerosols. This  
208 gradient is quantitatively defined as the rate of change of radiance with respect to TH:

$$209 \quad \mathbf{G}(\lambda, H) = \partial \ln \mathbf{I}(\lambda, H) / \partial H \quad (4)$$

210 As shown in Fig. 3a, the variation characteristics of radiance gradient with wavelength in the 500-900 nm provide a  
211 basis for determining cloud top height. In cloud-free conditions, the radiance intensity varies slightly with wavelength;  
212 whereas in the presence of clouds, the wavelength dependence of radiance is significantly stronger than that of aerosols.  
213 Based on this, in this study, the cloud top height is determined by calculating the spectral gradient difference, with the  
214 formula as follows:

$$215 \quad \ln \mathbf{R}(H) = [\mathbf{G}(\lambda_s, H) - \mathbf{G}(\lambda_l, H)] \quad (5)$$

216 where,  $\lambda_s$  and  $\lambda_l$  denote the short wavelength and long wavelength, respectively. In this study,  $\lambda_s$  is set to 674 nm, and  
217  $\lambda_l$  is set to 868 nm. The positive cloud detection threshold for LP data is 1.5, which is also applicable to the detection of  
218 polar mesospheric clouds (PMCs). Taking the SNPP satellite orbit 51220 on September 15, 2021 as an example (Fig.3b),  
219 the characteristics of  $\ln \mathbf{R}$  profiles differ significantly between two cloudy events and one cloud-free event: the  
220 maximum value of  $\ln \mathbf{R}$  in the cloud-free event is below 1.5, while that in the cloudy events is above this threshold, and  
221 the TH corresponding to the maximum  $\ln \mathbf{R}$  value is the cloud top height. Retrievals are not performed below the cloud  
222 top height, while the multiplicative update factor above the cloud top is propagated downward into the cloudy region.



223

224

225 **Figure 3.** Radiance gradient  $G(\lambda, H)$  and gradient difference  $\ln R$  during orbit 51220 on September 15, 2021. (a) Radiance gradient  
 226  $G(\lambda, H)$  spectrum at 3°N under different atmospheric conditions: clear sky (blue), cloud (red), and aerosol (green); (b) Radiance  
 227 gradient difference  $\ln R$  derived from OMPS/LP measurements for three equatorial events, showing the cloud detection results. The  
 228 black dashed line represents the threshold employed for cloud identification.

### 229 3.4 Implementation details

230 In this study, the SCIATRAN v2.2 toolbox (Rozanov et al., 2017) is employed as forward model to calculate the  
 231 simulated radiances required for ozone concentration retrieval. The observed and simulated radiances are processed  
 232 through normalization and wavelength pairing to form retrieval vectors, which serve as inputs to the MART algorithm to  
 233 drive the iterative update of ozone profiles.

234 The radiative transfer solution in the forward model is based on the discrete ordinate method applied to a spherical  
 235 atmosphere with a pseudo-spherical approximation for multiple scattering. The solution incorporates the effects of  
 236 multiple scattering and refraction while explicitly omitting polarization. Radiance calculations in the model are focused  
 237 solely on ozone, an absorbing gas, with the ozone absorption cross-sections taken from Bogumil et al. (2000). The  
 238 pressure and temperature profiles used in this study were obtained from the Global Modeling and Assimilation Office  
 239 (GMAO) interpolated dataset. These meteorological data are incorporated in the OMPS/LP L1G dataset provided by  
 240 NASA (NASA, 2025a). In addition, the model sets the stratospheric background aerosol type as LOWTRAN (Kneizys,  
 241 1988), the boundary layer humidity as 80%, and the boundary layer aerosol type as marine. The retrieved ozone profiles  
 242 are reported on the same vertical grid as the OMPS/LP L1G input data, which has a fixed spacing of 1 km in tangent  
 243 height. However, this sampling interval does not imply an equivalent effective vertical resolution. The true vertical  
 244 resolution is generally coarser than 1 km, particularly in regions of lower measurement sensitivity. The prior profiles are  
 245 from SCIATRAN's built-in database. These profiles are provided by McLinden climatology (C. McLinden,  
 246 Meteorological Service of Canada, personal communication) and include monthly and latitude-dependent vertical  
 247 distributions of volume mixing ratios for  $\text{O}_3$ ,  $\text{NO}_2$ ,  $\text{BrO}$ , and  $\text{OCIO}$ , as well as pressure and temperature in the 0 to 100  
 248 km altitude range.

## 249 4 Results

250 This section presents the processing results derived from the full year of 2021 OMPS-LP data. We utilized the L1G  
 251 v2.6 dataset (Jaross, 2023), which incorporates enhanced stray light correction and pointing accuracy as detailed in  
 252 Section 2.2. The analysis is based exclusively on measurements from the instrument's central slit.

## 253 4.1 Error analysis

254 In the field of error analysis on limb-scattering ozone retrieval, there is a wealth of academic studies. Zhu et al.  
255 (2022) used numerical perturbation to conduct formal error analysis on the retrieval method of the weighted  
256 multiplicative algebraic reconstruction technique, accurately quantifying ozone retrieval errors at different altitudes.  
257 Arosio et al. (2022) systematically evaluated random errors and systematic errors for stratospheric ozone profile retrieval  
258 based on OE algorithms. These research results provide important references for the error analysis of MART retrieval  
259 algorithm, and the error estimation results of this study are consistent with those in Arosio et al. (2022) and Zhu et al.  
260 (2022).

261 To ensure data quality, radiance measurements contaminated by clouds were systematically excluded during  
262 retrieval. Furthermore, the effective surface albedo was determined directly from OMPS/LP radiance measurements at  
263 675 nm (referred to as scene reflectance in the NASA product), and the corrected THs provided in the NASA L1G data  
264 were adopted. Accordingly, the retrieval error budget focuses on four primary sources: prior profiles, aerosols extinction  
265 profile, ozone absorption cross-sections, and measurement noise.

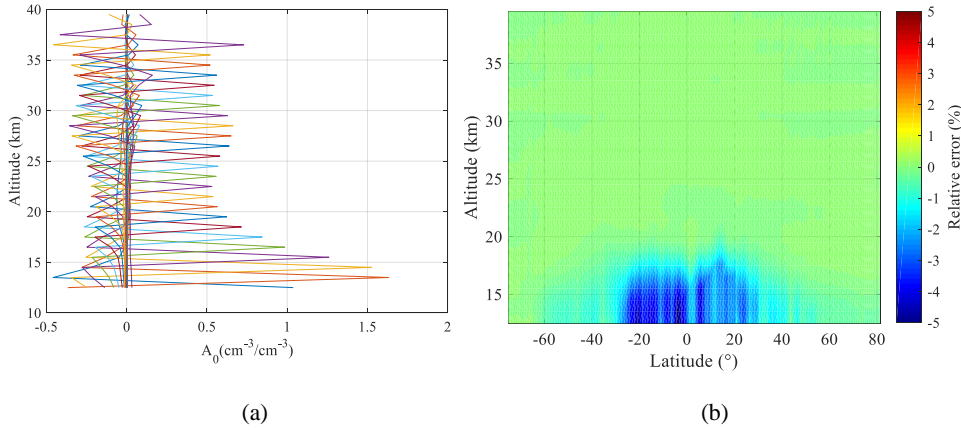
266 We assess the sensitivity of the retrieval to the prior profile through a perturbation-based approach. In this study, the  
267 prior sensitivity analysis matrix  $\mathbf{A}_0$  is used to quantify the sensitivity of retrieval to the prior profile, and its expression  
268 is as follows:

$$269 \mathbf{A}_0 = \frac{\partial \hat{\mathbf{x}}}{\partial \mathbf{x}_0} \quad (6)$$

270 where  $\mathbf{x}_0$  and  $\hat{\mathbf{x}}$  represent the initial ozone profile and the retrieved ozone profile, respectively. To calculate the column  
271 vectors of  $\mathbf{A}_0$ , the ozone concentration at a single altitude was perturbed in  $\mathbf{x}_0$  by 5% and analyzes the corresponding  
272 changes in  $\hat{\mathbf{x}}$ . Specifically,  $\partial \mathbf{x}_0$  is the perturbation applied to the prior, and  $\partial \hat{\mathbf{x}}$  is the difference between the retrieval  
273 using the perturbed prior and the retrieval using the unperturbed prior.  $\mathbf{A}_0$  is a dimensionless matrix, whose  
274 characteristics can intuitively reflect the impact of changes in the prior profile on the retrievals.

275 Fig. 4a illustrates the distribution of the prior sensitivity analysis matrix ( $\mathbf{A}_0$ ) column vectors across the 12–40 km  
276 altitude range, with each curve plotted at a vertical grid resolution of 1 km. A peak centered near the perturbation altitude  
277 indicates that the retrieval at that altitude retains sensitivity to the prior value at the same level. The width of the peak  
278 reflects the degree of vertical smoothing inherent in the retrieval. In the lower stratosphere (below 20 km), the response  
279 amplitudes are strong, indicating that strong prior dependence due to reduced measurement information content under  
280 weak limb-scattering signals. This is consistent with the reduced information content of limb measurements in the upper  
281 troposphere and lower stratosphere, where the retrieval is primarily constrained by the prior.

282 While Fig. 4a illustrates the pattern of prior influence, it does not quantify the actual retrieval error that would result  
283 from an inaccurate prior. To assess this, the entire prior profile was uniformly scaled by +5% at all altitudes, and the  
284 relative difference between the perturbed retrieval and the standard retrieval was computed. Fig. 4b shows the relative  
285 error induced by a +5% perturbation of the prior profile. Below 20 km, the retrieval shows sensitivity to the a priori, with  
286 relative errors  $-5\%$  in tropical regions. This indicates that a small increase in the prior profile leads to a noticeable  
287 underestimation of retrieved ozone concentrations in the tropical lower stratosphere, reflecting the high sensitivity of the  
288 retrieval to prior information in this region where measurement information content is low. With increasing altitude, the  
289 magnitude of the error progressively decreases. Above 25 km, the error approaches 0% across all latitudes, At high  
290 latitudes, the error magnitude remains relatively small at all altitudes, indicating weaker prior dependence compared to  
291 tropical and mid-latitude regions.



292

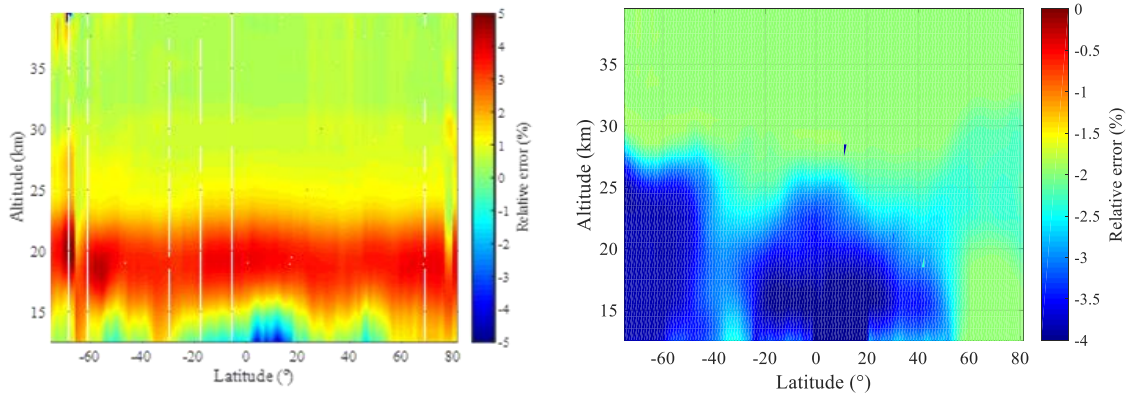
293

294 **Figure 4.** Examples of  $A_0$  (plotted every 1 km) and theoretical accuracy of prior profiles. (a) Distribution of  $A_0$  for measurements at  
 295 2.2 °S; (b) Relative retrieval error resulting from a uniform +5% perturbation of the entire prior profile (orbit 51220 on September 15,  
 296 2021).

297 The uncertainty of stratospheric aerosol extinction coefficients must be considered in the error budget for ozone  
 298 profile retrievals. Previous studies have shown that retrieved aerosol extinction profiles have an average upper error  
 299 bound of approximately 30% in the lower stratosphere (Arosio et al., 2022). To assess the impact of this uncertainty on  
 300 our ozone retrieval, we perturbed the climatological aerosol extinction profile by uniformly scaling it by +30% at all  
 301 altitudes and repeated the retrieval. The relative difference between the perturbed retrieval and the standard retrieval was  
 302 then computed. Fig. 5a depicts the resulting ozone retrieval errors as a function of latitude and altitude. It is evident that  
 303 retrieval errors induced by variations in aerosol extinction coefficients are predominantly distributed within the 15-25 km  
 304 altitude range, with a magnitude of approximately 5%, and errors in the southern high latitudes are more pronounced.  
 305 Within the 25-30 km range, the error is around 2%, while above 30 km, it is less than 1%. Below 15 km, errors vary with  
 306 latitude, mostly falling within the range of  $\pm 2\%$ .

307 The temperature dependence of ozone absorption cross-sections has the potential to introduce errors in the  
 308 retrieved profiles. To assess this effect quantitatively, we followed the approach which applied a uniform +2%  
 309 perturbations to the ozone absorption cross-sections at all temperatures used in the forward model. This perturbation  
 310 magnitude represents a typical conservative estimate of cross-section uncertainty in the Chappuis band (Arosio et al.,  
 311 2022). The retrieval was then repeated using the perturbed cross-sections, and the relative difference with respect to the  
 312 standard retrieval was computed.

313 As shown in Fig. 5b, the resulting retrieval error exhibits a distinct vertical and latitudinal structure. In the tropics,  
 314 the largest negative deviations ( $-3\%$  to  $-5\%$ ) appear below 20 km, indicating that retrievals in the tropical lower  
 315 stratosphere are most sensitive to uncertainties in ozone absorption cross-sections. In the Southern Hemisphere (SH)  
 316 mid-to-high latitudes, prominent negative deviations ( $-3\%$  to  $-4\%$ ) are found below 26 km. In the Arctic region, the  
 317 negative bias below 20 km is relatively smaller, at approximately  $-2\%$ . Across all latitudinal bands, the error stabilizes  
 318 near  $-2\%$  above 25 km. These results confirm that uncertainties in ozone absorption cross-sections introduce systematic  
 319 biases in lower stratospheric ozone retrievals, especially in the tropics and SH mid-to-high latitudes. Specifically, a  
 320 positive perturbation in the cross-sections leads to an underestimation of ozone concentrations, as observed in the  
 321 negative biases in Fig. 5b.



(a) (b)

**Figure 5.** Distribution of relative errors in ozone retrieval with latitude and altitude, resulting from: (a) a +30% uniform perturbation of the aerosol extinction profile; (b) a +2% uniform perturbation of ozone absorption cross-sections at all temperatures.

To quantify the impact of random measurement noise on retrieval precision, a Monte Carlo simulation was performed using data from OMPS/LP orbit 51220. Sixteen representative latitudes spanning from 80 S to 80 N were selected. For each latitude, Gaussian random noise with a standard deviation of 1% was added independently at each tangent height to the retrieval vector  $y_j$  (Eq. 2). This process was repeated 100 times, generating 100 independent noisy realizations per latitude. A full MART retrieval was conducted for each realization, producing an ensemble of 100 retrieved ozone profiles for each latitude. The random uncertainty due to measurement noise was quantified as the standard deviation of the 100 retrieved profiles at each altitude, expressed as a percentage of the average of the unperturbed profiles.

Fig. 6 shows the latitudinal and altitudinal distribution of the resulting random uncertainty. Uncertainty remains low (<10 %) at most latitudes within the 20–33 km mid-stratosphere, reflecting robust and stable retrieval performance. Above 30 km, especially at high latitudes, uncertainty increases sharply to above 20 %, which is mainly attributed to weaker signals in the visible spectral range. In the tropics below 20 km, a region of elevated uncertainty (>15 %) is identified, likely associated with low ozone abundances, strong atmospheric variability, or reduced information content from the measurements.

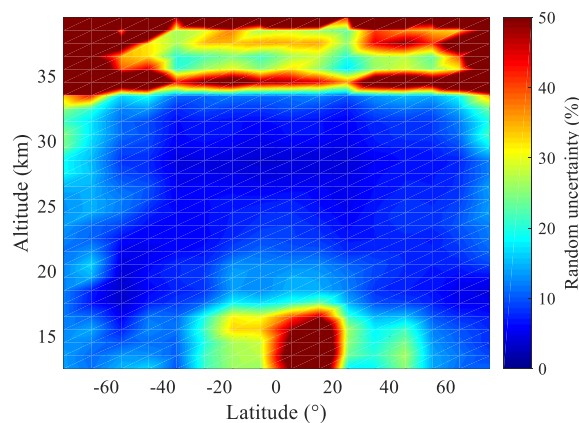


**Figure 6.** Random uncertainty in retrieved ozone profiles due to measurement noise, quantified as the standard deviation of 100 Monte Carlo realizations with 1% Gaussian noise added to the retrieval vector.

## 343 4.2 Comparison with NASA OMPS-LP ozone product

344 The OMPS/LP v2.6 ozone profile retrieval algorithm developed by the NASA team is built on wavelength pairing  
 345 and an optimal estimation with prior constraints (Kramarova and Deland, 2023). This algorithm operates on combined  
 346 UV-Vis measurement data from 12.5 km (or cloud top) to 57.5 km, producing a single ozone profile from each retrieval.  
 347 The measurement vectors are obtained via doublet and triplet methods, with specific parameters detailed in Table 1.  
 348 During algorithm implementation, the retrieved surface albedo, cloud top height, and corrected tangent height are  
 349 incorporated. In the forward model, aerosol extinction coefficients retrieved from OMPS/LP measured data are used. For  
 350 validation, only altitudes above the detected cloud top height are included in the comparison.

351 **Table 1.** Parameters used in the OMPS/LP v2.6 ozone algorithm, according to Kramarova and Deland, (2023).

Parameters	Values
Wavelength used in UV (nm)	295, 302, 306, 312, 317, 322, 353
Wavelength used in Vis (nm)	510, 606, 675
Normalization Altitude in UV (km)	60.5 km
Normalization Altitude in Vis (km)	40.5 km

352 Fig. 7 shows a comparison between the retrievals of this study and those of OMPS/LP v2.6, involving  
 353 approximately 770,000 profiles. Among them, Fig. 7a presents an example of number density for the annual average  
 354 profile, and Fig. 7b shows the relative differences of the annual data. In this study, the relative difference is calculated as  
 355 follows:

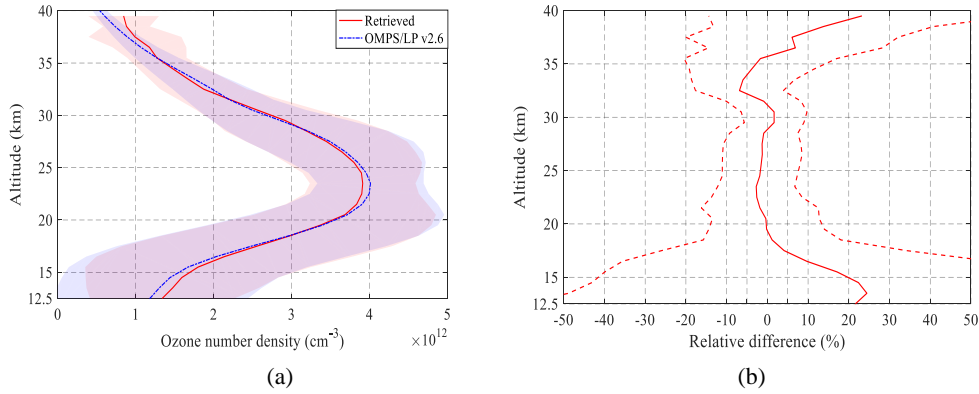
$$356 E_{\text{dif}} = \frac{2 \cdot ([O_3]_{\text{Ret}} - [O_3]_{\text{Ref}})}{([O_3]_{\text{Ret}} + [O_3]_{\text{Ref}})} \times 100\% \quad (7)$$

357 where  $[O_3]_{\text{Ret}}$  denotes the ozone profile retrieved in this study, and  $[O_3]_{\text{Ref}}$  represents the reference ozone profile  
 358 product.

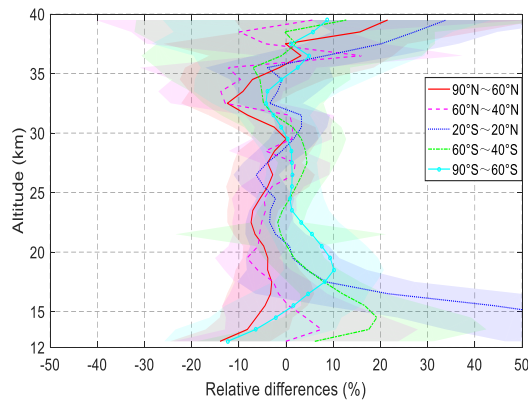
359 As presented in Fig. 7b, the ozone concentrations from our retrieval systematically exceed those of the OMPS/LP  
 360 v2.6 product at altitudes below 19 km and above 35 km. The positive deviation increases with decreasing altitude,  
 361 reaching a maximum of approximately 10–24% at the upper and lower retrieval boundaries. The ozone concentration is  
 362 slightly lower between 20 and 28 km, with a deviation within 3%. There is an inherent negative deviation of about -6%  
 363 around ~33 km. Overall, the deviation between 17 and 36 km is confined within 5%.

364 Fig. 8 shows the mean relative differences between the retrievals of this study and OMPS/LP v2.6 in tropical  
 365 regions and southern, northern mid-high latitudes. In the tropical regions within the 18-36 km altitude range, the  
 366 deviation is within 5%, showing good consistency. At northern mid-high latitudes, the difference between 12 and 32 km  
 367 reaches 8%, and the difference above 32 km is as high as 8–13%, with similar deviations in the Arctic region. In the  
 368 southern mid-high latitudes, most of the deviations above 18 km are less than 3%, but there is a positive deviation of up  
 369 to 19% near 15 km. In the Antarctic region, this positive deviation reaches approximately 10% around 18 km.

370 The two datasets differ significantly in the upper troposphere and lower stratosphere (UTLS) region, especially in  
 371 the tropical region, mainly due to the extremely low ozone concentration at this altitude. The large positive deviation at  
 372 the upper boundary of retrieval is caused by the decreased ability of the visible spectrum to retrieve ozone at high  
 373 altitudes, while the NASA product uses combined ultraviolet and visible spectrum information for retrieval at this  
 374 altitude. Although there are differences between the retrievals of this study and the OMPS/LP v2.6 product in terms of  
 375 ozone absorption cross-sections, prior profiles, aerosol settings, retrieval algorithms, and spectra, the overall consistency  
 376 is high.



377  
 378  
 379 **Figure 7.** (a) Annual mean ozone number density profiles from this study and OMPS/LP v2.6, with shaded areas indicating the  
 380 standard deviation. (b) The corresponding annual mean relative differences calculated pairwise for each collocated measurement using  
 381 Eq. (7), with the standard deviation shown as a dashed line.



382  
 383 **Figure 8.** Zonal mean relative differences (this study vs. OMPS/LP v2.6) across five latitudinal bands (60°–90° N, 40°–60° N, 20° S–  
 384 20° N, 60°–40° S, 90°–60° S); standard deviations are shown as shaded areas.

385 **4.3 Comparison with MLS**

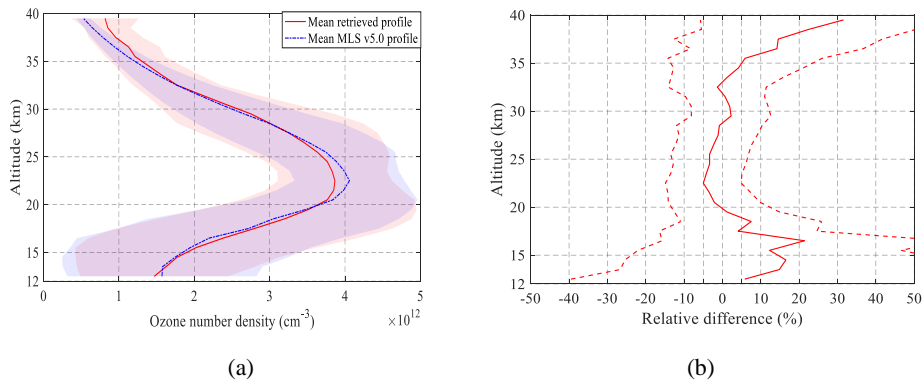
386 The Earth Observing System-Microwave Limb Sounder (EOS-MLS) aboard the Aura satellite was successfully  
 387 launched on July 15, 2004 (Waters et al., 2006). The satellite completes about 14 orbits daily, achieving global coverage  
 388 between 82° S and 82° N. MLS provides vertical ozone profiles from the upper troposphere to the middle atmosphere  
 389 using the 240 GHz frequency band by detecting naturally emitted microwave thermal radiation from the Earth's  
 390 atmospheric limb measurements. Detailed descriptions can be found by Waters et al. (2006).

391 For validation purposes, this study employs the latest MLS L2 version 5.0 data product (Schwartz et al., 2020), with  
 392 data filtering applied in accordance with the protocols recommended by Livesey et al. (2022). To ensure collocation  
 393 quality from the dataset, stringent criteria were enforced: we retained only those data pairs where the geographical  
 394 separation between the OMPS/LP and MLS footprints was within 1° in both latitude and longitude, and the observation  
 395 time difference was less than 6 hours. In cases where multiple MLS profiles corresponded to a single OMPS/LP  
 396 measurement, their average was computed and used. For consistent comparison with NASA products and ozonesonde  
 397 data, the MLS volume mixing ratio (VMR) and pressure were first transformed to number density and altitude, utilizing  
 398 the MLS geopotential height and temperature. These converted profiles were subsequently interpolated onto the regular  
 399 altitude grid of the OMPS retrievals using a spline method.

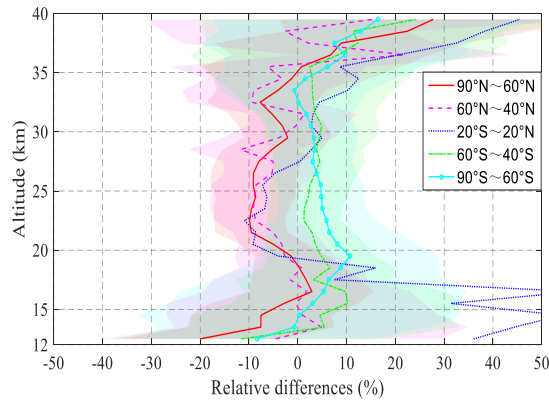
400 Fig. 9 presents the average profiles and relative differences between the retrieval results of this study and MLS v5.0,  
 401 involving approximately 93,000 profiles. The results show that compared with MLS v5.0, the ozone concentration

402 retrieved in this study has a relatively large positive deviation of 5–20% below 18 km; the positive deviation above 32  
 403 km increases with altitude; within the 18–35 km height range, the deviation between the two is confined within 5%.

404 Fig. 10 shows the mean relative differences in five latitude zones, with shaded areas indicating the standard  
 405 deviations. In terms of data sample size, there are approximately 18,000 profiles in the tropical region, about 20,000 in  
 406 the northern high latitudes, and around 15,000 in the southern high latitudes. The analysis results reveal that within the  
 407 12–35 km height range, the zonal average relative differences in each latitude zone are basically confined within 10%.  
 408 Among them, the northern mid-high latitudes exhibit a stable negative deviation of 5–10% at 20–35 km; the southern  
 409 mid-latitudes have a constant positive deviation of 1–5% at 18–36 km, which increases to 3–10% in the polar regions. In  
 410 the tropical regions the differences change sign with altitude: the retrieved ozone number density at 19–27 km is 5–10%  
 411 lower than that of MLS, while it is 3–10% higher in the 28–36 km range. It is worth noting that below 19 km, the  
 412 consistency between the retrieval results of this study and MLS data decreases significantly, with the relative difference  
 413 in the tropical region even exceeding 30%, although the absolute difference is relatively small (see Fig. 10a).



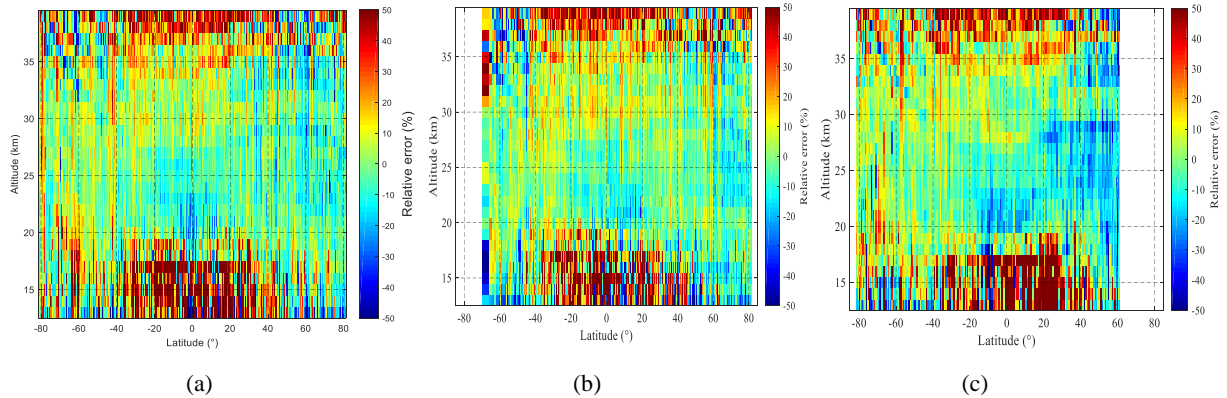
414  
 415  
 416 **Figure 9.** (a) Annual mean ozone number density profiles from this study and MLS v5.0, accompanied by standard deviations (shaded  
 417 areas). (b) The corresponding annual mean relative differences calculated pairwise for each collocated measurement using Eq. (7),  
 418 with the standard deviation shown as a dashed line.



419  
 420 **Figure 10.** Zonal mean relative differences for (this study vs. MLS v5.0) five latitudinal bands (60°–90° N, 40°–60° N, 20° S–20° N,  
 421 60°–40° S, 90°–60° S); standard deviations as shaded areas.

422 Fig. 11 depicts the altitude-dependent relative differences between retrieved profiles and MLS zonal means in 1°  
 423 latitude bins across the three selected periods. The full-year 2021 data shown in Fig. 11a indicate that within the 20–35  
 424 km altitude range, differences across all latitudes are basically confined within ±10%. The altitude-dependent behavior of  
 425 the retrieval biases can be summarized as follows. In the tropical UTLS region, oscillating differences exceeding 30% are  
 426 observed, which may be attributed to several factors: the highly dynamic variability of ozone concentrations, the limited  
 427 detection sensitivity at the lowest retrieval altitudes, and the influence of cloud filtering. Furthermore, the inherently low  
 428 ozone abundance in this region exacerbates the discrepancies in relative values. A distinct negative bias in retrieved

429 ozone values is evident at 20–23 km in the tropics, particularly pronounced during winter (Fig. 11c). Conversely, a  
 430 positive bias is observed over Antarctica, possibly linked to inaccuracies in the retrieved effective surface albedo,  
 431 particularly in polar regions with high seasonal variability. Above 35 km, the retrievals exhibit a positive bias in the  
 432 tropics. This bias arises from the inherently limited sensitivity of the visible spectrum at these altitudes, where ozone  
 433 absorption is weak and measurement signals become dominated by noise and stray light.



434  
 435  
 436 **Figure 11.** Relative differences in ozone number density, averaged over 1° latitude bins and plotted as a function of altitude, for (a) the  
 437 entire year of 2021, (b) the boreal summer months (June-August), and (c) December.

438 In summary, the comparative analysis of this study shows that the effectiveness of OMPS retrieval varies across  
 439 different regions and altitudes: the accuracy in tropical regions is concentrated in the 20-35 km altitude range; in  
 440 mid-latitude regions, good consistency is also observed below 15 km. Nevertheless, in some atmospheric regions and  
 441 under different seasonal conditions, the relative deviation may still exceed 10% compared with MLS data.

#### 442 4.4 Comparison with OSIRIS

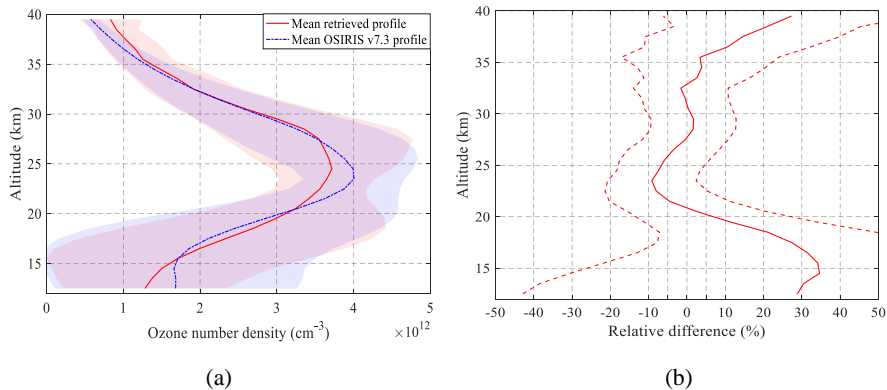
443 In February 2001, the OSIRIS instrument was launched aboard the Odin satellite into a nearly circular  
 444 sun-synchronous orbit (Llewellyn et al., 2004). The orbit has an altitude of approximately 600 km, an orbital period of 96  
 445 minutes, an inclination of 97.8°, and covers an observational latitude range from 82°S to 82°N. The satellite's ascending  
 446 node crosses the equator at approximately 18:00 local time. Detailed descriptions of the instrument can be found by  
 447 Llewellyn et al., (2004). Degenstein et al. (2009) used the MART to retrieve ozone profiles in the altitude range from 10  
 448 km or cloud top to 60 km, with the retrieval algorithm integrating radiation information from the UV and VIS bands. In  
 449 this study, the version of OSIRIS L2 v7.3 data (University of Saskatchewan, 2025) is used for verification.

450 Owing to the sparsity of coincident OSIRIS measurements, a relaxed collocation criterion was adopted. Data pairs  
 451 were considered matched if the geographical distance between the instrument footprints was within 2° in latitude and 5°  
 452 in longitude, and the time difference was within 24 hours. When multiple OMPS/LP profiles corresponded to a single  
 453 OSIRIS observation, their average was used. To unify the data format, the ozone concentration unit (mol/m<sup>3</sup>) of OSIRIS  
 454 profiles is converted to number density (molecule/cm<sup>3</sup>).

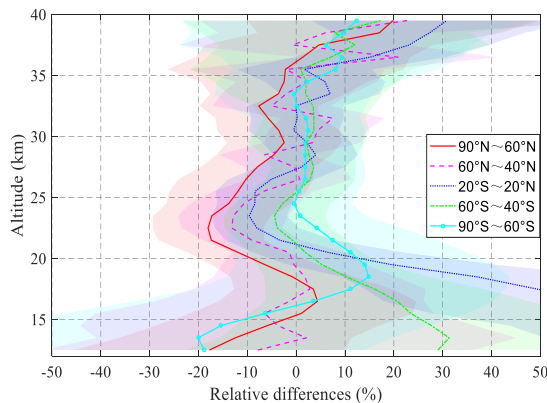
455 Fig. 12 shows the average profiles and relative differences between the retrieval results of this study and OSIRIS  
 456 v7.3, involving approximately 44,000 profiles. The results indicate that compared with OSIRIS v7.3, the ozone  
 457 concentration retrieved in this study has a relatively large positive deviation of 28-34% below 18 km; above 35 km, the  
 458 positive deviation increases with increasing altitude; in the 20-35 km altitude range, except near 23 km, most of the  
 459 deviations between the two are confined within 5%.

460 Fig. 13 further compares the mean relative differences of the five latitude zones, with shaded areas indicating the  
 461 standard deviations. In terms of data sample size, there are approximately 17,000 profiles in the tropical region, about  
 462 10,000 in the northern high latitudes, and around 7,000 in the southern high latitudes. The analysis shows that the

463 northern mid-high latitudes have a significant negative deviation of 5-13% at 21-25 km altitude, which is more prominent  
 464 in polar regions; the difference in the southern mid-latitudes at 20-36 km altitude is less than 4%, and the consistency in  
 465 the Antarctic region at 23-35 km altitude is better than 2.5%; most of the deviations in the tropical region at 26-36 km  
 466 altitude are within 2%. In addition, the differences in the region below 20 km are significant, with the relative difference  
 467 in the tropical region exceeding 50% and reaching 30% at 13 km in the southern mid-latitude zone.



468  
 469  
 470 **Figure 12.** (a) Annual mean ozone number density profiles from this study and OSIRIS v7.3, accompanied by standard deviations  
 471 (shaded areas); (b) The corresponding annual mean relative differences calculated pairwise for each collocated measurement using Eq.  
 472 (7), accompanied by standard deviations (dashed lines).



473  
 474 **Figure 13.** Zonal mean relative differences (this study vs. OSIRIS v7.3) for five latitudinal bands (60°-90° N, 40°-60° N, 20° S-20° N,  
 475 60°-40° S, 90°-60° S); standard deviations as shaded areas.

#### 476 4.5 Comparison with ozonesondes

477 To robustly validate the retrieved ozone concentrations at altitudes below 30 km, this study employs a comparative  
 478 analysis with ozonesonde measurements. The sonde data were obtained from the World Ozone and Ultraviolet Radiation  
 479 Data Centre (WOUDC) and the Southern Hemisphere Additional Ozonesondes (SHADOZ) network (Thompson et al.,  
 480 2007). Accounting for the sparse spatial distribution of ozonesonde stations, a relaxed collocation criterion was  
 481 implemented: an OMPS/LP measurement was considered a match if it fell within  $\pm 5^\circ$  latitude and  $\pm 10^\circ$  longitude of a  
 482 sonde station and occurred within  $\pm 12$  hours of its launch. For each ozonesonde profile, all collocated OMPS/LP  
 483 retrievals were averaged to form a single comparative data point.

484 In quantitative comparisons, to align the vertical resolution of ozonesonde data with that of OMPS data, a moving  
 485 average filtering method is used for dimensionality reduction of ozonesonde data. The specific procedure begins with  
 486 defining the window size of the moving average filter:

487 
$$N = \frac{\Delta z_{\text{low}}}{\Delta z_{\text{high}}} \quad (8)$$

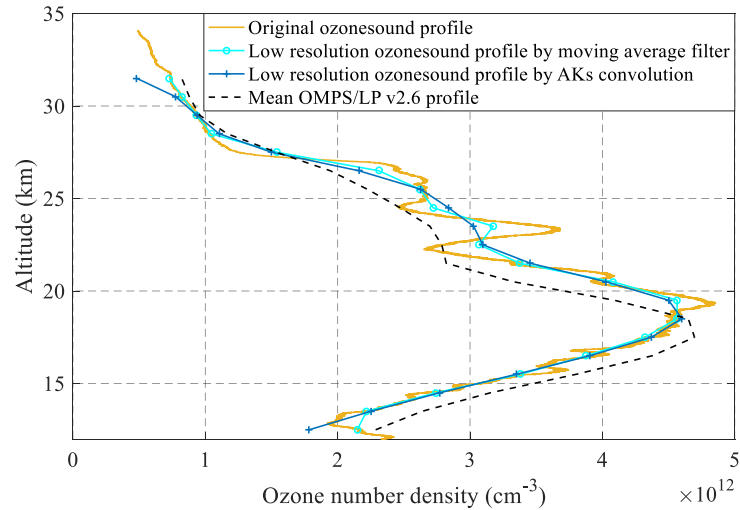
488 where,  $\Delta z_{\text{low}}$  and  $\Delta z_{\text{high}}$  represent the low vertical resolution of OMPS data and the high vertical resolution of  
 489 ozonesonde data, respectively.

490 Filtering is applied to the original ozonesonde data  $x_{\text{fine}}$  to obtain the dimensionality-reduced data  $x_{\text{coarse}}$ , which  
 491 is expressed as:

492 
$$x_{\text{coarse}}(z_k) = \frac{1}{2N+1} \sum_{j=-N}^N x_{\text{fine}}(z_{k+j}) \quad (9)$$

493 where  $z_k$  denotes the altitude, and  $k$  represents the layer index.

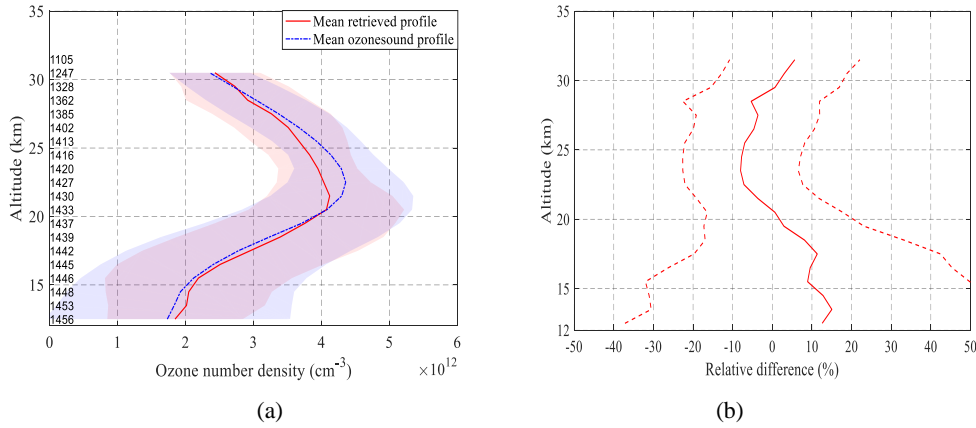
494 In addition, another processing approach involves convolving ozonesonde measurements with the averaging kernels  
 495 (AKs) retrieved from OMPS/LP v2.6 (see Arosio et al., (2018) for details). Taking the Alert station (82.5 N, 62.4 W) as  
 496 an example, Fig. 14 presents the comparison results between the ozonesonde data and the collocated OMPS average  
 497 profile on September 15, 2021. It is found that there are differences in the dimensionality-reduced ozonesonde data  
 498 obtained by the two methods. The data curve processed by convolution with averaging kernels is smoother and its shape  
 499 is closer to the OMPS product; while the data processed by moving average filter retains more original features with a  
 500 sharper curve. After comprehensive consideration, the moving average filter is finally adopted for data processing in this  
 501 study.



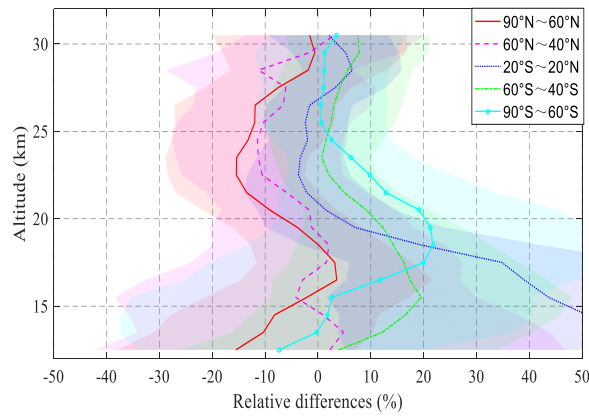
502  
 503 **Figure 14.** Ozonesonde data and OMPS collocated average profiles at Alert station on September 15, 2021.

504 Fig. 15 presents the annual average collocated profiles and their relative differences. The left side of the figure  
 505 indicates the number of valid collocations at each altitude, with the total sample size amounting to approximately 1460.  
 506 This study included data from 41 ozonesonde stations, involving over 1700 individual profiles. A significant positive bias  
 507 of 10–15% is observed in the retrievals compared to ozonesonde data below 18 km, while the deviation generally stays  
 508 within 10% across the 15–30 km altitude range.

509 Fig. 16 presents the mean relative differences across five latitude zones. The number of available collocations in the  
 510 tropical and Antarctic regions is approximately 200 and 75, respectively. Specifically, the tropical region shows good  
 511 consistency above 20 km, with most relative differences within  $\pm 4\%$  between 20 and 30 km. The southern mid-latitude  
 512 region also exhibits high consistency, with positive biases generally less than 5% above 20 km, but a relatively large  
 513 positive bias of about 19% near 15 km. In the Antarctic region, the bias is less than 2% above 25 km, while significant  
 514 differences occur below 25 km, with a positive bias as high as 21% at 19 km. The northern mid-latitude zone has a bias  
 515 of less than 5% below 21 km, but a constant negative bias of 5–11% between 21–28 km, and this negative bias is more  
 516 pronounced in the Arctic region.



517  
 518  
 519 **Figure 15.** (a) Annual mean collocated ozone number density profiles from this study and ozonesonde measurements, accompanied by  
 520 standard deviations (shaded areas). (b) Mean relative differences calculated pairwise for each collocated measurement using Eq. (7),  
 521 accompanied by standard deviations (dashed lines).



522  
 523 **Figure 16.** Zonal mean relative differences (this study vs. ozonesondes) for five latitudinal bands (60°–90° N, 40°–60° N, 20° S–20° N,  
 524 60°–40° S, 90°–60° S); standard deviations as shaded areas.

525 **5. Conclusions**

526 This study innovatively applies an ozone profile retrieval method—originally developed at the University of  
 527 Saskatchewan for OSIRIS measurements and based on wavelength pairing and the MART—to OMPS/LP observations.  
 528 After processing and analyzing the 2021 annual OMPS/LP v2.6 L1G data, observations with the instrument's central slit  
 529 and solar zenith angle less than 85° were selected, and ozone profiles between 12.5 and 39.5 km were retrieved. A  
 530 comprehensive multi-dimensional validation was conducted.

531 Comparison with the NASA L2 v2.6 official product shows that the overall consistency is good across latitude zones  
 532 at 20–36 km, with most differences within ±5%. However, differences near 33 km in the northern mid-latitudes and polar  
 533 regions reach up to 10%. Below 20 km, ozone concentrations are relatively high in the Antarctic ozone peak region, with  
 534 a pronounced positive bias around 15 km in tropical and southern mid-latitude zones.

535 Validation against MLS v5.0 and OSIRIS v7.3 ozone profiles, as well as ozonesonde data from SHADOZ and  
 536 WOUDC, indicates that relative differences with MLS are mostly within ±10% between 13 and 35 km, except for  
 537 significant discrepancies in the tropical UTLS region. Compared to OSIRIS v7.3, a negative bias of 13–18% occurs at  
 538 20–25 km in northern mid-high latitudes, while positive biases reach 18% at 18 km over Antarctic and exceed 20% at 15

539 km in southern mid-latitudes, with more pronounced deviations in the tropics. Relative to ozonesonde data, differences in  
540 tropical and southern mid-latitude regions at 20-30 km remain within  $\pm 4\%$ , whereas differences of 11-15% are observed  
541 at 20-25 km in northern mid-high latitudes. Consistency is good below 20 km in northern mid-latitudes, but positive  
542 biases reach 21% at 18 km over Antarctica and 19% at 15 km in southern mid-latitudes.

543 Overall, compared with the reference products, the retrieved ozone concentrations in this study exhibit biases mostly  
544 within 5% between 25 and 35 km. A negative bias of 5-10% is observed at 20-25 km in northern mid-high latitudes,  
545 particularly in the Arctic. Retrieved values are about 10% higher at the altitude of the Antarctic ozone concentration peak,  
546 10–15% higher at 15 km in southern mid-latitudes, and over 30% higher below 20 km in the tropics.

547 The identified biases mainly originate from three factors. Below 20 km, cloud effects remain non-negligible. A  
548 sensitivity test on a representative profile (equatorial region) demonstrates that, at the same altitudes above the CTH, our  
549 method—which propagates the multiplicative update factor from above the cloud top into the cloudy region—produces  
550 ozone concentrations approximately 25% higher than the scheme with retrieval limited only to altitudes above the cloud  
551 top. This result quantitatively reveals the potential systematic impact of cloud constraints on ozone profile retrievals  
552 under cloudy conditions. These discrepancies are further exacerbated by low ozone abundance, strong dynamical  
553 variability in the tropics, and the reduced sensitivity of limb retrievals at lower altitudes, while inconsistencies between  
554 the background aerosols used in retrievals and real atmospheric conditions also contribute. Beyond aerosol effects,  
555 additional bias contributions arise from ozone absorption cross-sections that incompletely account for  
556 temperature-dependent uncertainties, as well as the neglect of NO<sub>2</sub> absorption in the current forward model. The  
557 overestimation of ozone abundances above 35 km across all latitudes results from the limited sensitivity of the visible  
558 spectrum for high-altitude ozone retrievals, in contrast to the operational product that employs combined ultraviolet and  
559 visible spectral information.

560 Based on these findings, several priorities for follow-up research are identified. First, integrating operational aerosol  
561 extinction products from NASA will be essential to replace the current climatological approach and reduce systematic  
562 biases in the UTLS region. Further model improvements will include updating the ozone absorption cross-section  
563 database and incorporating NO<sub>2</sub> absorption into the forward model. Second, including ultraviolet channels will improve  
564 retrieval accuracy above 35 km, where visible-only measurements have low sensitivity. Third, refining cloud filtering  
565 will better constrain lower altitude retrievals. Finally, the consistent retrieval core shared with OSIRIS lays a solid  
566 technical foundation for constructing long-term, coherent stratospheric ozone records, thereby minimizing discrepancies  
567 in multi-satellite data merging and supporting climate studies that require stable, multi-decadal observational records.

## 568 **Data availability**

569 Ancillary information and v2.6 L1G OMPS/LP data were downloaded from <https://disc.gsfc.nasa.gov/datasets>  
570 (NASA, 2025a), where L2 data are also available. For the validation sections, MLS L2 data were also taken from <https://disc.gsfc.nasa.gov/datasets>  
571 (Schwartz, et al., 2020). OSIRIS v7.3 data were taken from  
572 <https://research-groups.usask.ca/osiris/data-products.php> (University of Saskatchewan, 2025). WOUDC data were  
573 downloaded on 10 April 2025 from <https://woudc.org/data/explore.php>. A list of all contributors is available on the  
574 following website: <https://woudc.org/contributors/>. SHADOZ data were downloaded on 21 April 2025 from  
575 <https://tropo.gsfc.nasa.gov/shadoz/Archive.html> (NASA, 2025b).

576 **Author contributions**

577 FZ designed the retrieval algorithm to OMPS/LP observations, processed the data set, performed the validation of  
578 the results and wrote the manuscript. FZ and SWL proposed the research and lead the project, analyzed the results and  
579 contributed to the writing of the manuscript and the scientific outcomes. XPL contributed the algorithm for cloud filtering,  
580 and reviewed the paper. FQS supervised and guided the retrieval process and reviewed the paper.

581 **Competing interests**

582 The authors declare that they have no conflict of interest.

583 **Acknowledgements**

584 This work was supported by the National Science Foundations of China (Grant No. 41875040), and partially funded  
585 by the Excellent Research and Innovation Team of Anhui Provincial Department of Education (2023AH010043)

586 We would like to express our sincere gratitude to the NASA OMPS SIPS team for providing data support. We are  
587 also thankful to the SCIATRAN radiative transfer model development team.

588 **References**

589 Arosio, C., Rozanov, A., Malinina, E., Eichmann, K., von Clarmann, T., and Burrows, J. P.: Retrieval of ozone profiles  
590 from OMPS limb scattering observations, *Atmos. Meas. Tech.*, 11, 2135–2149,  
591 <https://doi.org/10.5194/amt-11-2135-2018>, 2018.

592 Arosio, C., Rozanov, A., Gorshelev, V., Laeng, A., and Burrows, J. P.: Assessment of the error budget for stratospheric  
593 ozone profiles retrieved from OMPS limb scatter measurements, *Atmos. Meas. Tech.*, 15, 5949–5967,  
594 <https://doi.org/10.5194/amt-15-5949-2022>, 2022.

595 Bernath, P. F., McElroy, C. T., Abrams, M. C., Boone, C. D., Butler, M., Camy-Peyret, C., Carleer, M., Clerbaux, C.,  
596 Coheur, P. F., Colin, R., DeCola, P., De Mazière, M., Drummond, J. R., Dufour, D., Evans, W. F. J., Fast, H., Fussen,  
597 D., Gilbert, K., Jennings, D. E., Llewellyn, E. J., Lowe, R. P., Mahieu, E., McConnell, J. C., McHugh, M., McLeod, S.  
598 D., Michaud, R., Midwinter, C., Nassar, R., Nichitiu, F., Nowlan, C., Rinsland, C. P., Rochon, Y. J., Rowlands, N.,  
599 Semeniuk, K., Simon, P., Skelton, R., Sloan, J. J., Soucy, M.-A., Strong, K., Tremblay, P., Turnbull, D., Walker, K. A.,  
600 Walkty, I., Wardle, D. A., Wehrle, V., Zander, R., and Zou, J.: Atmospheric Chemistry Experiment (ACE): Mission  
601 overview, *Geophysical research letters*, 32, L15S01, <https://doi.org/10.1029/2005GL022386>. 2005.

602 Bertaux, J. L., Kyrola, E., Fussen, D., Hauchecorne, A., Dalaudier, F., Sofieva, V., Tamminen, J., Vanhellemont, F.,  
603 Fanton d'Andon, O., Barrot, G., Mangin, A., Blanot, L., Lebrun, J. C., Perot, K., Fehr, T., Saavedra, L., Leppelmeier,  
604 G. W., and Fraisse, R.: Global ozone monitoring by occultation of stars: an overview of GOMOS measurements on  
605 ENVISAT, *Atmos. Chem. Phys.*, 10, 12091–12148, <http://doi.org/10.5194/acp-10-12091-2010>, 2010.

606 Bogumil, K., Orphal, J., and Burrows, J. P.: Temperature dependent absorption cross sections of O<sub>3</sub>, NO<sub>2</sub>, and other

607 atmospheric trace gases measured with the SCIAMACHY spectrometer, in: Proceedings of the  
608 ERS-Envisat-Symposium, Goteborg, Sweden, 2000.

609 Burrows, J., Hölzle, E., Goede, A., Visser, H., and Fricke, W.: SCIAMACHY–Scanning imaging absorption spectrometer  
610 for atmospheric cartography, *Acta Astronautica*, 35, 445–451, [https://doi.org/10.1016/0094-5765\(94\)00278-T](https://doi.org/10.1016/0094-5765(94)00278-T), 1995.

611 Cisewski, M., Zawodny, J., Gasbarre, J., Eckman, R., Topiwala, N., Rodriguez-Alvarez, O., Cheek, D., Hall S.: The  
612 Stratospheric Aerosol and Gas Experiment (SAGE III) on the International Space Station (ISS) Mission, in:  
613 Proceedings 9241, Sensors, Systems, and Next-Generation Satellites XVIII, SPIE Remote Sensing, Amsterdam,  
614 Netherlands, <https://doi.org/10.1117/12.2073131>, 2014.

615 Chen, Z., DeLand, M., and Bhartia, P. K.: A new algorithm for detecting cloud height using OMPS/LP measurements,  
616 *Atmos. Meas. Tech.*, 9, 1239–1246, <https://doi.org/10.5194/amt-9-1239-2016>, 2016.

617 Chipperfield, M. P. and Bekki, S.: Opinion: Stratospheric ozone–depletion, recovery and new challenges, *Atmos. Chem.*  
618 *Phys.*, 24, 2783–2802, <https://doi.org/10.5194/acp-24-2783-2024>, 2024.

619 Degenstein, D. A., Bourassa, A. E., Roth, C. Z., and Llewellyn, E. J.: Limb scatter ozone retrieval from 10 to 60 km  
620 using a multiplicative algebraic reconstruction technique, *Atmos. Chem. Phys.*, 9, 6521–6529,  
621 <https://doi.org/10.5194/acp-9-6521-2009>, 2009.

622 DeLand, M., Bhartia, P., Xu, P., Kramarova, N., and Zhu, T.: OMPS Limb Profiler Ozone Product O<sub>3</sub>: Version 2.5 Data  
623 Release Notes, 2017.

624 Flittner, D. E., Bhartia, P. K., and Herman, B. M.: O<sub>3</sub> Profiles Retrieved from Limb Scatter Measurements: Theory,  
625 *Geophysical research letters*, 27(17), 2601–2604, <https://doi.org/10.1029/1999GL011343>, 2000.

626 Flynn, L., Long, C., Wu, X., Evans, R., Beck, C., Petropavlovskikh, I., McConville, G., Yu, W., Zhang, Z., Niu, J., Beach,  
627 E., Hao, Y., Pan, C., Sen, B., Novicki, M., Zhou, S., and Seftor, C.: Performance of the ozone mapping and profiler  
628 suite (OMPS) products, *J. Geophys. Res.-Atmos.*, 119, 6181–6195, <https://doi.org/10.1002/2013JD020467>, 2014.

629 Jia, J., Rozanov, A., Ladstätter-Weißmayer, A., and Burrows, J. P.: Global validation of SCIAMACHY limb ozone data  
630 (versions 2.9 and 3.0, IUP Bremen) using ozonesonde measurements, *Atmos. Meas. Tech.*, 8, 3369–3383,  
631 <https://doi.org/10.5194/amt-8-3369-2015>, 2015.

632 Jaross, G., Bhartia, P. K., Chen, G., Kowitt, M., Haken, M., Chen, Z., Xu, P., Warner, J., Kelly, T.: OMPS Limb Profiler  
633 instrument performance assessment, *J. Geophys. Res.-Atmos.*, 119, 4399–4412, <https://doi.org/10.1002/2013JD020482>,  
634 2014

635 Jaross, G.: OMPS-NPP L1G LP Radiance EV Wavelength-Altitude Grid swath orbital 3slit V2.6, Greenbelt, MD, USA,  
636 Goddard Earth Sciences Data and Information Services Center (GES DISC), Accessed: February 10, 2024,  
637 <https://doi.org/10.5067/YVE3FSNJ59RQ>, 2023.

638 Kneizys, F. X.: Users Guide to LOWTRAN 7[M]. Air Force Geophysics Laboratory, 1988.

639 Kramarova, N. A., Nash, E. R., Newman, P. A., Bhartia, P. K., McPeters, R. D., Rault, D. F., Seftor, C. J., Xu, P. Q., and  
640 Labow, G. J.: Measuring the Antarctic ozone hole with the new Ozone Mapping and Profiler Suite (OMPS), *Atmos.*  
641 *Chem. Phys.*, 14, 2353–2361, <https://doi.org/10.5194/acp-14-2353-2014>, 2014.

642 Kramarova, N. A., Pawan K. Bhartia, Glen Jaross, Leslie Moy, Philippe Xu, Zhong Chen, Matthew DeLand, Lucien  
643 Froidevaux, Nathaniel Livesey, Douglas Degenstein, Adam Bourassa, Kaley A. Walker, and Patrick Sheese. Validation  
644 of ozone profile retrievals derived from the OMPS LP version 2.5 algorithm against correlative satellite measurements.  
645 *Atmos. Meas. Tech.*, 11, 2837–2861, <https://doi.org/10.5194/amt-11-2837-2018>, 2018.

646 Kramarova, N. A., Xu, P., Mok, J., Bhartia, P. K., Jaross, G., Moy, L., Weaver, C., Frith, S., Ziemke, J., Chen, Z., Kahn,  
647 D., Nyaku, E., Li, J., Davis, S., and Jia, Y.: Ten Year Ozone Profile Record From Suomi NPP OMPS Limb Profiler,  
648 National Oceanic and Atmospheric Administration Washington D.C., District of Columbia, United States, Technical  
649 Review NASA Peer Committee December 21, 2022.

650 Kramarova, N. A.: OMPS-NPP L2 LP Ozone (O<sub>3</sub>) Vertical Profile swath daily Center slit V2.6, Greenbelt, MD, USA,

651 Goddard Earth Sciences Data and Information Services Center (GES DISC), Accessed: November, 2023,  
652 10.5067/8MO7DEDYTBH7, 2023.

653 Kramarova, N. A., and DeLand, M.: OMPS Limb Profiler Ozone Product O3: Version 2.6 Data Release Notes, 36pp,  
654 2023.

655 Kramarova, N.A., Xu, P., Mok, J., Bhartia, P. K., Jaross, G., Moy, L., Chen, Z., Frith, S., DeLand, M., Kahn, D., Labow,  
656 G., Li, J., Nyaku, E., Weaver, C., Ziemke, J., Davis, S., and Jia, Y.: Decade-long Ozone Profile Record from Suomi  
657 NPP OMPS Limb Profiler: Assessment of Version 2.6 Data, *Earth and Space Science*, 11, e2024EA003707,  
658 <https://doi.org/10.1029/2024EA003707>, 2024.

659 Li, F., Newman, P. A., and Waugh, D. W.: Impacts of stratospheric ozone recovery on southern ocean temperature and  
660 heat budget, *Geophysical Research Letters*, 50(18), e2023GL103951, <https://doi.org/10.1029/2023GL103951>, 2023.

661 Li, Z., Bi, J., Hu, Z., Ma, J., Li, B.: Regional transportation and influence of atmospheric aerosols triggered by Tonga  
662 volcanic eruption, *Environmental Pollution*, 325, 121429, <https://doi.org/10.1016/j.envpol.2023.121429>, 2023.

663 Livesey, N. J., Read, W. G., Wagner, P. A., Froidevaux, L., Santee, M. L., Schwartz, M. J., Lambert, A., Millán Valle, L.  
664 F., Pumphrey, H. C., Manney, G. L., Fuller, R. A., Jarnot, R. F., Knosp, B. W., and Lay, R. R.: Version 5.0x Level 2 and  
665 3 data quality and description document, available at: [https://mls.jpl.nasa.gov/data/v5-0\\_data\\_quality\\_document.pdf](https://mls.jpl.nasa.gov/data/v5-0_data_quality_document.pdf)  
666 (last access: June 10, 2025), 2022.

667 Llewellyn, E. J., Lloyd, N. D., Degenstein, D. A., Gattinger, R. L., Petelina, S. V., Bourassa, A. E., Wiensz, J. T., Ivanov,  
668 E. V., McDade, I. C., Solheim, B. H., McConnell, J. C., Haley, C. S., von Savigny, C., Sioris, C. E., McLinden, C. A.,  
669 Griffioen, E., Kaminski, J., Evans, W. F. J., Puckrin, E., Strong, K., Wehrle, V., Hum, R. H., Kendall, D. J. W.,  
670 Matsushita, J., Murtagh, D. P., Brohede, S., Stegman, J., Witt, G., Barnes, G., Payne, W. F., Piché L., Smith, K.,  
671 Warshaw, G., Deslauniers, D.-L., Marchand, P., Richardson, E. H., King, R. A., Wevers, I., McCreath, W., Kyrđ ä E.,  
672 Oikarinen, L., Leppelmeier, G. W., Auvinen, H., M égie, G., Hauchecorne, A., Lef èvre, F., de La N öe, J., Ricaud, P.,  
673 Frisk, U., Sjöberg, F., von Sch éle, F., and Nordh, L.: The OSIRIS Instrument on the Odin Spacecraft, *Canadian*  
674 *Journal of Physics*, 82(6), 411-422, <https://doi.org/10.1139/p04-005>, 2004.

675 Moy, L., Bhartia, P. K., Jaross, G., Loughman, R., Kramarova, N., Chen, Z., Taha, G., Chen, G., and Xu, P.: Altitude  
676 registration of limb-scattered radiation, *Atmos. Meas. Tech.*, 10, 167–178, <https://doi.org/10.5194/amt-10-167-2017>,  
677 2017.

678 NASA: OMPS data, available at: <https://disc.gsfc.nasa.gov/datasets>, last access: February 2025a.

679 NASA: SHADOZ data, available at: <https://tropo.gsfc.nasa.gov/shadoz/Archive.html>, last access: March 2025b.

680 Qian, Y. Y., Luo, Y. H., Zhou, H. J., Yang, T. P., Xi, L., and Si, F. Q.: First Retrieval of Total Ozone Columns from EMI-2  
681 Using the DOAS Method, *Remote Sensing*, 16(5): 1234-1245, <https://doi.org/10.3390/rs15061665>, 2024.

682 Rault, D. F. and Loughman, R. P.: The OMPS Limb Profiler Environmental Data Record Algorithm Theoretical Basis  
683 Document and Expected Performance, *Ieee Transactions on Geoscience and Remote Sensing*, 51(5): 2505-2527,  
684 <https://doi.org/10.1109/TGRS.2012.2213093>, 2013.

685 Rodgers, C. D.: Inverse methods for atmospheric sounding: theory and practice. Vol. 2. World scientific, 2000.

686 Roth, C. Z., Degenstein, D. A., Bourassa, A. E., and Llewellyn, E. J.: The retrieval of vertical profiles of the ozone  
687 number density using Chappuis band absorption information and a multiplicative algebraic reconstruction technique,  
688 *Canadian Journal of Physics*, 85(11), 1225-1243, <https://doi.org/10.1139/p07-130>, 2007.

689 Rozanov, V. V., Dinter, T., Rozanov, A. V., Wolanin, A., Bracher, A., and Burrows J.P.: Radiative transfer modeling  
690 through terrestrial atmosphere and ocean accounting for inelastic processes: Software package SCIATRAN. *Journal of*  
691 *Quantitative Spectroscopy & Radiative Transfer*, 194, 65-85, <https://doi.org/10.1016/j.jqsrt.2017.03.009>, 2017.

692 Schwartz, M., Froidevaux, L., Livesey, N., and Read, W.: MLS/Aura Level 2 Ozone (O3) Mixing Ratio V005, Greenbelt,  
693 MD, USA, Goddard Earth Sciences Data and Information Services Center (GES DISC), Accessed: June 10, 2025,  
694 <https://doi.org/10.5067/Aura/MLS/DATA2516>, 2020.

695 Thompson, A. M., Witte, J. C., Smit, H. G., Oltmans, S. J., Johnson, B. J., Kirchhoff, V. W., and Schmidlin, F. J.: Southern  
696 Hemisphere Additional Ozonesondes (SHADOZ) 1998–2004 tropical ozone climatology: 3. Instrumentation,  
697 station-to-station variability, and evaluation with simulated flight profiles, *J. Geophys. Res.-Atmos.*, 112,  
698 <https://doi.org/10.1029/2005JD007042>, 2007.

699 University of Saskatchewan: OSIRIS data. available at: <https://research-groups.usask.ca/osiris/data-products.php>, last  
700 access: July 25, 2025.

701 Veefkind, J. P., de Haan, J. R., Brinksma, E. J., Kroon, M., and Levelt, P. F.: Total ozone from the Ozone Monitoring  
702 Instrument (OMI) using the DOAS technique, *Ieee Transactions on Geoscience and Remote Sensing*, 44(5):  
703 1239-1244, <https://doi.org/10.1109/TGRS.2006.871204>, 2006.

704 von Clarmann, T., Degenstein, D. A., Livesey, N. J., Bender, S., Braverman, A., Butz, A., Compernelle, S., Damadeo, R.,  
705 Dueck, S., Eriksson, P., et al.: Overview: Estimating and reporting uncertainties in remotely sensed atmospheric  
706 composition and temperature, *Atmospheric Measurement Techniques*, 13(8), 4393-4436, 2020.

707 Waters, J.W., Froidevaux, L., Harwood, R. S., Jarnot, R. F., Pickett, H. M., and Read, W. G.: The Earth Observing System  
708 Microwave Limb Sounder (EOS MLS) on the Aura satellite, *Ieee Transactions on Geoscience and Remote Sensing*,  
709 44(5), 1075-1092, <https://doi.org/10.1109/TGRS.2006.873771>, 2006.

710 Xu, P. Q., Bhartia, P. K., Jaross, G. R., DeLand, M. T., Larsen, J. C., Fleig, A., Kahn, D., Zhu, T., Chen, Z., Gorkavyi, N.,  
711 Warner, J., Linda, M., Chen, H. G., Kowitt, M., Haken, M., and Hall, P.: Release 2 data products from the Ozone  
712 Mapping and Profiling Suite (OMPS) Limb Profiler, *Proc. SPIE 9242, Remote Sensing of Clouds and the Atmosphere*  
713 *XIX, and Optics in Atmospheric Propagation and Adaptive Systems XVII*, 92420K (17 October 2014),  
714 <https://doi.org/10.1117/12.2067320>, 2014.

715 Young, P. J., Harper, A. B., Huntingford, C., Paul, N. D., Morgenstern, O., Newman, P. A., Oman, L. D., Madronich, S.,  
716 and Garcia, R. R.: The Montreal Protocol protects the terrestrial carbon sink, *Nature* 596, 384–388,  
717 <https://doi.org/10.1038/s41586-021-03737-3>, 2021.

718 Zawada, D. J., Rieger, L. A., Bourassa, A. E., and Degenstein, D. A.: Tomographic retrievals of ozone with the OMPS  
719 Limb Profiler: algorithm description and preliminary results, *Atmos. Meas. Tech.*, 11, 2375–2393,  
720 <https://doi.org/10.5194/amt-11-2375-2018>, 2018.

721 Zhu, F., Li, S.W., Yang, T. P., and Si, F. Q.: Research on Inversion and Application of Ozone Profile Based on OMPS  
722 Limb Scattering Observation, *Acta Optica Sinica*, 45(6), 82-92, <https://doi.org/10.3788/AOS202141.0401005>, 2025.

723 Zhu, F., Si, F. Q., Zhan, K., Dou, K., and Zhou, H. J.: Inversion of Ozone Profile of Limb Radiation in Chappuis-Wulf  
724 Band. *Acta Optica Sinica*, 41(4), 39-48, <https://doi.org/10.3788/AOS241244>, 2021.

725 Zhu F., Si, F. Q., Zhou, H. J., Dou, K., Zhao, M. J., and Zhang, Q.: Sensitivity Analysis of Ozone Profiles Retrieved from  
726 SCIAMACHY Limb Radiance Based on the Weighted Multiplicative Algebraic Reconstruction Technique, *Remote*  
727 *Sensing*, 14(16), 3954, <https://doi.org/10.3390/rs14163954>, 2022.

728  
729  
730  
731  
732  
733  
734  
735